INFLUENCE OF ARBITRARY VORTICAL WAKE EVOLUTION ON FLOWFIELD AND NOISE GENERATION OF HELICOPTER ROTORS

A.J. Spyropoulos[+], A.P. Fragias[+], D.P. Margaris[#], D.G. Papanikas[*]
[*]Professor Dr-Ing, [#]Assist. Prof. Dr-Eng, [+]Dipl.-Eng., Fluid Mechanics Lab., Mechanical Engineering and Aeronautics Department, University of Patras, GR-26500, Patras, Greece,
e-mail: spyrop@mech.upatras.gr

Keywords: *helicopters, rotor aerodynamics, rotor aeroacoustics*

Abstract

This paper presents a combined methodology consisting of rotor aerodynamic and aeroacoustic computation modules. Aerodynamic calculations utilise the Vortex Element Method for the description of free vortex wake, which determines the rotor flowfield. The mathematical model discretizes the wake into vortex elements. The induced velocity is calculated for the distorted wake geometry, by means of the Biot-Savart law, integrated in closed form over each of these elements. Bound circulation variations and unsteady blade airloading are computed as a result of the nonuniform induced downwash. Wake roll up process, vortex core modelling, vorticity dissipation, blade section boundary layer growth are incorporated in numerical modelling of aerodynamic computations. Computed blade loading variations are used as the basis of loading noise predictions. Aeroacoustic analysis concentrates on helicopter rotor noise prediction in time domain. The formulation is based on the Ffowcs-Williams and Hawkings (FW-H) equation modelling only thickness and loading noise by integrating monopole and dipole sources over the blade surface at subsonic tip speeds. The developed computational procedure demonstrates the influences of the highly complicated rotor flowfield to noise generation. Blade airloading, acoustic and sound pressure level results are demonstrated and compared with experimental data, showing a fairly good agreement between measurements and predictions.

1 Introduction

The flowfield in the wake area behind an advancing or hovering rotor is highly unsteady and three dimensional, dominated by interacting vortical flows. These flows are mainly generated by the vorticity shed from the rotor blades. On a real rotor, as the trailing vortices created from each individual blade evolve, they distort under the action of their interacting induced velocity fields. This distortion changes the shape of an otherwise helical vortex filament and is responsible for the nonuniform induced downwash on the rotor disk and the vibratory airloading. The interactions between rotor blades and wake vortices, the abrupt variations of blade loading as well as the variety of flow regimes observed on rotor disk, produce an increased emission of aerodynamic rotor noise. By these means, an efficient calculation of rotor wake flow and the nonuniform induced downwash on rotor disk together with a reliable blade flowfield simulation are the basic tools for a less-noise-generating or "quite" helicopter rotor design.

The complexity of the flow pattern and the arbitrary motion of the vortex filaments makes the accurate calculation of the rotor induced downwash difficult. In addition several phenomena taking place in rotor wake such as vortex core growth and decay, core bursting and blade vortex interactions are not yet thoroughly understood. This has led to simplified wake modelling such as the prescribed wake geometry and the uniform inflow assumption [14] with the corresponding loss of accuracy. On the other hand the need of a deeper insight

in the physical mechanisms of the above phenomena was the motivation of numerous experimental works, contacted with model or full scale rotors [4,12,17,25].

In the work presented here, rotor aerodynamic simulations are based on a free wake analysis which employs the Vortex Element Method (VEM) coupled with airloads calculation module applying both lifting line and lifting surface methods. The blade motion calculations include provisions for articulated or hingeless blades, along with specific cases, where the main blade flapping modules can be regarded separately or coupled. Taking advantage of the flexible physical modelling of VEM, various models extracted from experimental observations, which represent viscous vortex core behaviour [17,27], can be incorporated in wake computations. The present analysis assumes that the helicopter rotor performs a steady state equilibrium flight, implying that forward flight speed, rotor rotational speed, tip path plane orientation and wake geometry remain constant with time.

Rotor aeroacoustic analysis is based on the acoustic analogy concept [18] which relies upon the solution of Ffowcs-Williams and Hawkings [9] equation. This equation combines the three source terms, thickness, loading and quadrupole, which are related to different noise generation mechanisms. In subsonic hover and forward flight conditions, the noise radiation is computed in terms of monopole and dipole sources [6,9]. The quadrupole source is important especially in transonic flow for the prediction of high-speed impulsive (HSI) noise and it is not taken into account for the purely subsonic conditions of present analysis.

The computational procedure gives the possibility to study rotor aerodynamics and aeroacoustic problems, with good time efficiency and transparency in the analysis of local flow phenomena, where other specialised methods can be applied for extended study. The experimental data used for comparisons include test cases executed during cooperative European research programs on rotorcraft aerodynamics and aeroacoustics performed in the open test section of the German-Dutch Wind Tunnel (DNW) The Netherlands [25].

2 Rotor aerodynamic analysis

2.1 Rotor wake modelling

Free wake concept is a continuous improving methodology which during recent years research has became a powerful aerodynamic tool for the prediction of rotor induced flowfield [5,13,22]. An integrated computational procedure has been developed for an efficient calculation of rotor downwash distribution based on wake geometry predicted by a free wake simulation using the Vortex Element Method (VEM) [21]. Based on this procedure, present work extends the mathematical modelling and couples with an aeroacoustic module for rotor noise predictions.

The vorticity in rotor wake is distinguished by VEM regarding its source in two main parts, the trailing and the shed vorticity. Spanwise circulation variations on rotor blade generate trailing vorticity, g_n, whose direction is parallel to the local flow velocity. On the other hand azimuthal variations produce shed vorticity radially oriented, g_s, due to the transient nature of the rotor blade flowfield (figure 1).

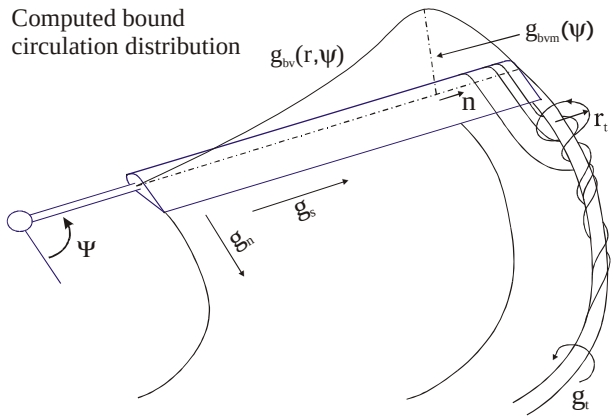

Figure 1. Rotor wake physicomathematical modelling

Depending on its strength and its spanwise origin, the wake vorticity can form either concentrated vortex tubes or spread vortex layers. The objective of VEM is to simulate these formations of vorticity with simple elements, in order to predict the velocity field induced on the rotor disk and in the wake itself.

For this purpose, the whole of the vortical wake is simulated with a multitude of discrete straight or curved vortex lines and vortex sheets. These elements are allowed to move freely and decay, leading to distorted wake geometry under the action of the resulting velocity field. This way, the use of specific models to represent the distribution and behaviour of vorticity is allowed by VEM in an effective free wake calculation scheme.

Circulation conservation dictates that the strength of the vorticity shed at specific spanwise locations behind each rotor blade is determined by the circulation gradients on the blade. Since it is difficult to predict the exact analytical function of the circulation distribution on the rotor blades, a representative model must be applied. The initial strength of every vortex element used, is derived from this bound circulation model. In general, the bound circulation has a peak near the blade tip while it becomes zero at the tip. This steep gradient creates a high strength trailing vortex sheet, which rapidly rolls up and forms the concentrated tip vortex.

Due to its strength, tip vortex dominates rotor wake flowfield and makes the modelling of tip vortex roll up process an important aspect in wake aerodynamics.

For the present analysis the roll up model of a vortex sheet trailing from a fixed wing is applied [3] which is verified in rotor aerodynamics by experimental results as already well documented [24]. The applicability of this model to rotor wake analysis is based on the conservation of bound circulation $g_{bv}(r)$ as it is transferred to the tip vortex circulation $g_t(r_t)$. According to this model, for vortex core radii fulfilling the equation

$$r_t = \frac{1}{g_{bv}(r)} \int_1^r \frac{dg_{bv}(n)}{dn} n\, dn - r \qquad (1)$$

the circulation is defined as $g_t(r_t)=g_{bv}(r)$, where n is a spanwise coordinate with a range of $n=0$ (location of maximum bound circulation) to $n=1$ (blade tip radius). In this way, circulation within radius r_t from vortex centre is equalised with bound circulation at radial coordinate r, when equation (1) is valid. Since the above model concerns purely potential flow, vortex core radius or any viscous effects cannot be predicted.

With tip vortex circulation defined by the roll up model, the numerical implementation of roll up process consists of a vortex sheet at the blade tip area just behind the blade, which is gradually decreasing in width till it forms a concentrated vortex tube (figure 1). After roll up process, the resulting tip vortex filament is numerically represented by vortex line segments, whose circulation can be constant or linearly varying.

In contrast with tip vortex, the main characteristic of inboard vorticity shed at blade's wake, is the formation of thin layers which are spread as long as blade span. The origin of this part of wake vorticity is the radial and azimuthal bound circulation variation for the trailing and shed wake respectively. Implementation of VEM leads to the representation of these parts of rotor wake either with vortex lines or vortex sheets [21]. Vortex line modelling is computationally simpler but it requires an artificially large vortex core radius to avoid unrealistic blade vortex interaction phenomena. This model is used for preliminary calculations while for detailed analysis the vortex sheet model is applied which, although time consuming, is in closer agreement with the physical description of these wake parts.

2.2 Induced velocity calculations

The wake model applied by VEM and the bound circulation distribution are in close relation since the circulation strength of every vortex wake element is defined by conservation from this circulation distribution. For the wake model where both trailing and shed wake along with the origin of tip vortex (roll up portion) are represented with vortex sheets, the bound circulation model is shown in figure 2.

As can be seen in the picture, the inboard trailing vortex sheet extending from point A to C behind the rotor blade, has a constant circulation radially since bound circulation is assumed to vary linearly at this part of the blade. The rolling up tip vortex sheet extending

from point D to E has also a radially constant circulation which is a fraction of the total tip vortex circulation for early ages $g_{ts}(f)=f_{ts}(f)\, g_{bv}(f)$ where g_{ts} is the circulation of the tip vortex sheet and f is vortex element's age.

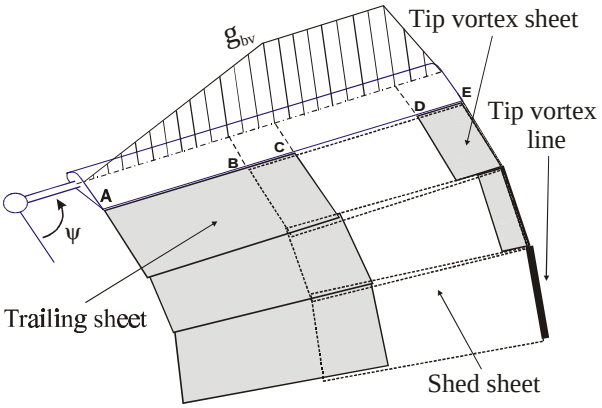

Figure 2. Schematic representation of bound circulation model and wake vortex elements for early ages

The factor f_{ts} in the above relation is a function of azimuth angle and can be changed externally in order to investigate the efficiency of the roll up modelling compared to experimental observations. The circulation variation along the azimuthal direction for both trailing and tip vortex sheets, depends on the use of either a vortex line or vortex sheet for the shed wake simulation [21]. When a sheet element is used for the shed wake (figure 2), their circulation changes linearly in azimuthal direction. In both cases the shed vortex element extending from point B to E has a radially constant circulation distribution. The radial location of points B, C, E is internally derived from the bound circulation distribution at each azimuthal step.

Since the present analysis concerns basically potential flowfield, the fundamental induced velocity calculations are based on the Biot-Savart law. Because of rotor wake flowfield complexity, the calculation of downwash induced on rotor disk has always been a tempting challenge for aerodynamic engineers. Early attempts were made with simplified approaches such as the rigid or semi-rigid assumption for wake vortices geometry [1,2,26]. Only for such simplified approaches is possible to calculate wake-induced downwash with a direct numerical integration of the Biot-Savart law over the whole wake. The above methods give usable results only in specific cases and empirical parameters extracted from experiments are necessary. The utilisation of discrete singularity elements (vortex lines and sheets) by VEM for rotor wake simulation, has the advantage of converting the direct integration in a closed form integration of the Biot-Savart law over the known spatial locations of these elements. With a reasonable step of discretisation, the simplification that is made to the actual wake geometry can be overcome.

The contribution of a vortex line segment to the induced velocity at an arbitrary point in space is given by the relation

$$\vec{w}_{ij} = -\frac{1}{4p}\int \frac{g_i\left(\vec{r}_{ijm} - k\cdot\vec{e}_k\right)\times d\vec{k}}{\left|\vec{r}_{ijm} - k\cdot\vec{e}_k\right|^3} \qquad (2)$$

where $\vec{r}_{ijm}$ is the minimum distance from the vortex line i to the point j, $\vec{e}_k$ the unit vector in the direction of the vortex segment, g_i the strength of the vortex segment and k the coordinate measured along the vortex segment.

As described in previews paragraph, the formation of the trailing and shed vorticity can be simulated by a series of vortex sheets that follow the initially helical shape of the rotor wake. The Biot-Savart relation for a surface distribution of vorticity is

$$\vec{v} = -\frac{1}{4p}\int \frac{\vec{r}\times\vec{w}}{r^3} dA \qquad (3)$$

where $\vec{w}$ is the vorticity vector on the vortex surface. For the vortex sheets included in the present analysis some geometrical expressions can be derived by inspection of figure 3 as follows

$$\vec{r} = \vec{r}_m - s\vec{e}_k - t\vec{e}_l\,,\quad \vec{w} = g_k\vec{e}_k - g_l\vec{e}_l$$

where g_k, g_l is the vorticity strength along k and l directions respectively, $\vec{r}_m$ is the minimum distance of point P from the vortex sheet plane,

$\vec{e}_k, \vec{e}_l, \vec{e}_n$ are orthogonal unit vectors with origin at the centre of the sheet and $\vec{s}, \vec{t}$ are orthogonal unit vectors with origin at point *M*.

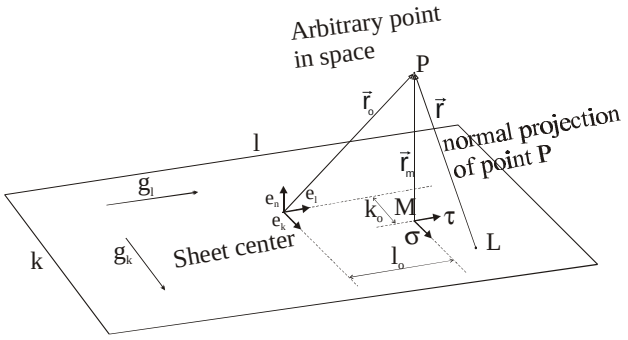

Figure 3. Vortex sheet induced velocity notation

With these expressions substituted to the Biot-Savart law of equation (3), the expression for evaluating the velocity induced by a plain rectangular vortex sheet to an arbitrary point in space is derived below

$$\vec{v} = -\frac{1}{4p}\int_{l_o-(l/2)}^{l_o+(l/2)}\int_{k_o-(k/2)}^{k_o+(k/2)} \frac{r_m g_k \vec{e}_l - r_m g_l \vec{e}_k}{(r_m^{\,2}+s^2+t^2)^{3/2}} + \frac{(tg_k - sg_l)\vec{e}_n}{(r_m^{\,2}+s^2+t^2)^{3/2}} dsdt \qquad (4)$$

where $\vec{r}_o$ is the position vector of point *P* from the centre of the sheet, $k_o = -\vec{r}_o \cdot \vec{e}_k$ and $l_o = -\vec{r}_o \cdot \vec{e}_l$

In general the vortex sheet can have linearly varying vorticity strength along both of its side edges. In case where the sheet has a linearly varying circulation along one of its edges and a constant distribution along the other, a valid expression can be obtained by eliminating the corresponding terms in the above relation. Since the induced velocity calculations based on equation (4) are computationally complicated, another approach can be used preliminary, by representing the inboard trailing and the shed vorticity, is with straight vortex line elements having an enlarged effective vortex core [21].

2.3 Rotor blade dynamics

Rotor blade dynamic behaviour is important for downwash computations, to the extent that influences the angle of attack distribution seen by the blade, and therefore alters the bound circulation distribution. Due to out-of-plane motion, rotor blade balances the asymmetry of rotor disk loading. For low speed forward flight cases such as considered here, where the objective remains on studying the influence of rotor wake on rotor aerodynamics and aeroacoustics, the introduction of blade elasticity through flapwise bending with a simple mode shape, improves the computations to the extent that wake geometry is affected by blade bending deflection.

For basic computations the simplification of rigid flapping motion was found adequate. The momentum equilibrium about the flapping hinge (with offset *e*) of an articulated rotor, assuming a hinge spring K_b, results to the rigid flap equation, with *b* being the flapping degree of freedom

$$\int_e^R mh\ddot{b}(r-e)dr + \int_e^R mW^2 rhbdr + K_b(b-b_p) = \int_e^R (r-e)F_z dr \qquad (5)$$

where *W* is the angular velocity, *m* the blade mass per unit length, *h=(r-e)/(1-e)* the rigid flapping mode shape, *r* the radial coordinate, b_p a precone angle and F_z a generalised aerodynamic force acting on blade section at radial distance *r* from the blade hinge. The spring constant K_b can simulate a hingeless rotor (K_b=¥) or a fully articulated (K_b=*0*)

For more detailed computations the out-of-plane flapwise bending is considered and the partial differential equation that governs the blade motion is derived by taking the equilibrium of aerodynamic, inertial and structural bending moments at an arbitrary location r on the blade

$$\frac{d^2}{dr^2}\left(EI\frac{d^2z}{dr^2}\right) - \frac{d}{dr}\left(\int_r^R mW^2 y\,dy\,\frac{dz}{dr}\right) + m\ddot{z} = F_z \qquad (6)$$

where *E* is the modulus of elasticity of the blade section, *I* the modulus-weighted area moment about the chordwise principal axis and *y* the radial coordinate outboard the *r* location on the

blade. The out-of-plane deflection $z(r,t)$ can be written as a series of normal modes describing the spanwise deformation. In general

$$z(r,t)=\sum_{k=1}^{\infty} n_k(r)q_k(t) \qquad (7)$$

where n_k is the mode shape and $q_k(t)$ is the corresponding degree of freedom. For the developed computational procedure two modes were found suitable for the desirable accuracy of blade motion solution. The first one is the above mentioned rigid body flapping mode, and the second mode is given as $n=4r^2-3r$ which is appropriate if blade's basic bending deformation [14], is considered.

With assumed mode shapes, two linearised equations occur with q_1, q_2 degrees of freedom as unknown quantities and their time (azimuth) derivatives included in specific terms. After calculating out-of-plane blade deflections and their time derivatives, a new angle of attack distribution on rotor disk is obtained taking into account blade sections local normal velocities.

3 Rotor aeroacoustic analysis

The physicomathematical modelling of rotor noise emission for the present analysis, is based on the Lighthill acoustic analogy, as extended by Ffowcs-Williams and Hawkings (FW-H) [9] for sound generated by surfaces in arbitrary motion. In generalised form [8] the FW-H equation is expressed in the following inhomogeneous wave equation

$$\Box^2 p'(\vec{x},t)=\frac{1}{a^2}\frac{\partial^2 p'}{\partial t^2}-\nabla^2 p'= \\ =\frac{\partial}{\partial t}\left[r_0 v_n|\nabla S|d(S)\right]-\frac{\partial}{\partial x_i}\left[\ell_i|\nabla S|d(S)\right]+ \\ +\frac{\partial^2}{\partial x_i x_j}\left[T_{ij}H(S)\right] \qquad (8)$$

where p' is the acoustic pressure, v_n the local normal velocity on the rotor blade surface, ℓ_i the force on the medium per unit area, $T_{ij}=\rho u_i u_j+p'\delta_{ij}-\tau_{ij}-a^2\rho'\delta_{ij}$ the Lighthill stress tensor, δ and H are the Dirac and Heaviside functions, τ_{ij} the viscous stress and r_0, a the density and the speed of sound in the undisturbed medium respectively.

The overall amount of the acoustic pressure generated by the rotor blade consists of three main components in the right side equation (8). These terms are related to thickness, loading and quadrupole noise sources respectively. The rotor blade is defined by the equation S = 0.

Thickness and loading noise are computed by integrating monopole and dipole sources over the blade surface, while quadrupole noise is calculated over the whole volume of the fluid domain. High speed impulsive noise, which is caused mainly by turbulence, viscosity and transonic flow singularities, is represented by the quadrupole term in the computational procedure. However, in rotors rotating under subsonic flow conditions, this term has a minor importance due to the fact that it is at least an order of magnitude less than the other terms. Therefore, in the present paper only thickness and loading noise terms of the FW-H equation are utilised, while the quadrupole source is considered negligible.

Several solutions of the FW-H equation have been developed retaining only thickness and loading source terms. Thus, for open helicopter rotating blades, discussed in this paper, the acoustic formulation is given by the following set of equations [7,8,10]

$$4\pi p'_T(\vec{x},t)=\sum_{k=1}^{N}\left[\left[\frac{r_0\dot{v}_n}{r(1-M_r)^2}\right]_{ret}\right]_k\cdot DS_k \\ +\sum_{k=1}^{N}\left[\left[\frac{r_0 v_n\left(r\dot{M}_i\hat{r}_i+aM_r-aM^2\right)}{r^2(1-M_r)^3}\right]_{ret}\right]_k\cdot DS_k \qquad (9)$$

$$4\pi p'_L(\vec{x},t)=\frac{1}{a}\sum_{k=1}^{N}\left[\left[\frac{\dot{\ell}_i\hat{r}_i}{r(1-M_r)^2}\right]_{ret}\right]_k\cdot DS_k+ \\ +\sum_{k=1}^{N}\left[\left[\frac{\ell_r-\ell_i M_i}{r^2(1-M_r)^2}\right]_{ret}\right]_k\cdot DS_k+ \\ +\frac{1}{a}\sum_{k=1}^{N}\left[\left[\frac{\ell_r\left(r\dot{M}_i\hat{r}_i+aM_r-aM^2\right)}{r^2(1-M_r)^3}\right]_{ret}\right]_k DS_k \qquad (10)$$

where, p'_T and p'_L are the thickness and loading noise respectively. The magnitude v_n represents the local velocity of the blade surface in the direction normal to *S=0*, ℓ_r is the component of the local force acting on the fluid, due to the blade in the radiation direction, M and a are the local Mach number and speed of sound in the undisturbed medium. The terms inside the integrals are calculated for the retarded time, *t*, i.e. the emission time. The dot over a symbol implies differentiation of this magnitude in respect to emission time. The integrals with *1/r* and $1/r^2$ dependence are the far field and near field terms, respectively.

Thickness noise calculations depend on the strength and distribution of monopole sources on the blade surface, which are purely geometric. However, dipole sources, affecting loading noise, are defined by the airloads distribution over the blade, according to the helicopter flight condition and the airfoil geometric and aerodynamic characteristics. The above analysed formulation is valid for arbitrary airfoil and blade characteristics and gives results of acceptable accuracy for subsonically rotating helicopter rotors.

4 Vortex core modelling

Any computational procedure for rotor wake analysis includes a numerical representation of tip vortex structure and evolvement in the wake environment. A great deal of the current knowledge about these important aerodynamic issues has been derived mainly from experimental measurements. As a result empirical relations are commonly used for the determination of critical parameters for tip vortex physical modelling such as the vortex core radius, the velocity distribution at the core region and the viscous core growth.

Since VEM is based on a potential field solution such as Biot-Savart law for the calculation of the velocity induced by vortex elements to arbitrary points in space, singularities are expected to occur close to these elements. Due to the absence of viscosity effects, the velocity calculated in close proximity to these elements tends to be infinite. In order to remove these singularities and model the effects of viscosity in a convenient way the vortex core concept is introduced.

The core radius is defined as the distance from the core centre where the maximum tangential velocity is observed. A corresponding expression for the radial circulation distribution inside the core region is introduced in the computations, which alters the velocity induced from a vortex element. Outside the core region the induced velocity has an approximately potential distribution which tends to coincide with the Biot-Savart distribution fairly away from the vortex line.

Several experimental and theoretical works have been presented [4,25,28] where velocity measurements have been taken in the core region and corresponding radial circulation distributions have been extracted. According to Vatistas [27] a series of tangential velocity profiles in the vortex core is given by the relation

$$V_q(r) = \frac{g\, r}{2p\left(r_c^{2n} + r^{2n}\right)^{1/n}} \qquad (11)$$

where *g* is the circulation of the vortex line, *n* is an integer variable, *r* is the radial distance from the vortex centre and r_c is the core radius. Using this relation for different values of *n*, the velocity profiles of some well-known core models can be derived using the nondimensional radius $\bar{r} = r/r_c$. For *n=1* the core model of references [15,24] is derived

$$V_q(\bar{r}) = \frac{g}{2pr_c}\frac{\bar{r}}{(1+\bar{r}^2)} \qquad (12)$$

For *n=2* the model proposed in reference [17] by Bagai-Leishman is derived

$$V_q(\bar{r}) = \frac{g}{2pr_c}\frac{\bar{r}}{\sqrt{1+\bar{r}^4}} \qquad (13)$$

Vortex core radius was found to be between 5-7% of blade chord. A comparison of the above two vortex core models as well as Rankine and Lamp-Oseen [16] models, which

were fitted in a least-square sense with experimental data, is given in [17]. The Kaufmann-Scully core model, is slightly underestimating the peak tangential velocity at early wake ages and improving later while the Bagai-Leishman vortex was in best agreement with experiments between the four models. With the application of vortex core circulation distribution, the velocity induced by the vortex elements is altered. Using the Kaufmann-Scully model the velocity induced to a point *j* from a finite straight vortex line segment *i*, of constant circulation g_i, with arbitrary orientation considering the relative geometrical distances $\vec{r}_{i1,j}$,$\vec{r}_{i2,j}$, is given as

$$\vec{w}_{i\,j} = \frac{g_i}{4p}\,\vec{r}_{i1,j} \times \vec{r}_{i2,j}\,\frac{N}{D} \qquad (14)$$

where

$$N = \left(\left|\vec{r}_{i1,j}\right| + \left|\vec{r}_{i2,j}\right|\right)\left[1 - \left(\vec{r}_{i1,j}\;\vec{r}_{i2,j}\right)\Big/\left(\left|\vec{r}_{i1,j}\right|\left|\vec{r}_{i2,j}\right|\right)\right]$$

$$D = \left|\vec{r}_{i1,j}\right|^2\left|\vec{r}_{i2,j}\right|^2 - \left(\vec{r}_{i1,j}\;\vec{r}_{i2,j}\right)^2 +$$

$$+ r_c^2\left(\left|\vec{r}_{i1,j}\right|^2 + \left|\vec{r}_{i2,j}\right|^2 - 2\,\vec{r}_{i1,j}\;\vec{r}_{i2,j}\right)$$

For the present computational procedure both of the above core models were included as comparable options to describe the core of line and sheet vortex elements. The effect of viscosity on real vortices is to diffuse the vorticity and to create a vortex core that increases its diameter until there is a balance by the inward velocity component. The decaying nature of a viscous vortex can be represented by the following relation which is a solution of Navier-Stokes equation:

$$V_q = \frac{g_0}{2pr}\cdot\left(1 - exp\left(-r^2/4nt\right)\right) \qquad (15)$$

where V_q is the vortex tangential velocity, g_0 the initial total circulation of the vortex, *r* the radial distance from the vortex centreline, *t* the time, and *n* the kinematic viscosity coefficient. Equation (15) is a solution for the laminar vortex due to Oseen. The variation of r_c with time which result from equation (15) must be modified to incorporate turbulence effects by a turbulent viscosity coefficient *l* as $r_c = r_o + 0.00855\sqrt{tl}$ [16].

This relation is derived assuming $n=1.46\ x\ 10^{-5}\ m^2\ s^{-1}$ with r_o being the initial core radius. The effect of *l* is an additional growth of the core than that of the laminar case (*l=1*). Before the first blade passage experienced by the vortex, when there is an enlargement of the core radius, viscous core growth can have a significant effect on calculated induced velocities on rotor blades.

5 Blade vortex interactions and arloading calculations

Local intersections of rotor blades with wake vortices can result to extensive disturbances of blade bound circulation and surface pressure distribution. As a result these phenomena, widely mentioned as Blade Vortex Interactions (BVI), have an important contribution to rotor blade unsteady airloads and are responsible for impulsive noise generation. When such an interaction takes place some main effects have been experimentally observed [24,28].

The near-passing vortex experiences a sharp increase of its diameter while its total circulation is conserved. This sharp increase is so dramatic that is often mentioned as vortex core "bursting". The result is a decrease of the velocity induced by this specific vortex filament after the age of bursting. A second effect is that the bound circulation distribution is also altered when a concentrated vortex passes in close proximity to a rotor blade. The change of circulation produces an additional shedding of vorticity in the near wake, which in terms affects the induced velocity distribution on the rotor blade in an opposite manner than this of the concentrated vortex. To account for these near wake effects, a formula based on a simplified lifting surface method proposed by Johnson [13], has been adopted. According to it, due to the interaction of the blade with a tip vortex passing nearly enough to cause remarkable downwash changes, a correction is made to the velocity induced at blade radial stations by the interacting vortex.

With the numerical implementation of the above described aerodynamic phenomena in free wake calculations, a reliable rotor induced downwash distribution is obtained. Sequentially, blade section angle of attack distribution can be computed by the relation

$$a(r,y) = q(r) - tan^{-1}(U_P / U_T) \qquad (16)$$

where U_P is the air velocity perpendicular to No Feathering Plane (NFP) which includes nonuniform rotor downwash, U_T is the tangential velocity to blade airfoil at a radial station, both normalised by tip speed *WR*, and *q(r)* is the collective pitch angle.

With known angle of attack and local chordwise in-plane velocity, a blade-element type methodology can be applied for blade section lift calculations. To evaluate the reliability of such a methodology, estimation for radial flow effects on rotor blades is necessary. For a conventional rotor blade, the spanwise, or secondary flow in the boundary layer is usually very small, especially in the turbulent part of the layer where the high turbulent stress hinders the radial flow. The order of magnitude of the radial velocity component for a blade of chord c=0.5 m rotating with *W=4 rps* can be estimated as $W \times c = 2p \times n \times c = 2p \times 4 \times 0.5 = O(10)$ whereas the free stream chordwise velocity is of the order of two hundred. The corresponding momentum in the boundary layer in the radial direction is more easily counterbalanced by the larger stresses in the turbulent layer than the small stresses in the laminar one. This physical fact is also confirmed by the boundary layer analysis of the rotating disk [23]. Thus, the radial flow velocities in the boundary layer of the blade do not play a major role since laminar flow regions on rotor blades are limited to the front part of about one third of the chord. Therefore, two dimensional boundary layer computations over blade sections can be regarded as satisfactory for analysis purposes [19].

For the computational procedure regarded here, an inviscid/viscous coupled scheme is adopted for blade section lift calculation. A panel method has been developed for the calculation of the potential field around an airfoil. This formulation represents airfoil's contour by a multitude of panel segments. A combination of source and doublet singularities is regarded for every panel and a Dirichlet type boundary condition is utilised in order to determine the strengths of the singularity elements. With known element strength, the flow potential function *F(x,y)* is determined and by differentiating tangentially to airfoil contour, the potential velocity distribution is obtained. For subsonic flows, compressibility effects are taken into account through the application of Prandtl-Glauert transformation rule.

The potential velocity distribution is imposed as a boundary condition to an integral boundary layer method [23]. This method is based on the simultaneous integration of the Von-Karman equation (eq. 17) for compressible boundary layer flow and the kinetic energy equation (eq. 18).

$$\frac{d\delta_2}{dx} + \delta_2\left(\frac{H_{12}+2}{U}\frac{dU}{dx} - \frac{M^2}{U}\frac{dU}{dx} + \frac{1}{r}\frac{dr}{dx}\right) = \frac{\tau_w}{\rho_r U^2} = \frac{c_f}{2} \qquad (17)$$

$$\frac{d\delta_3}{dx} + \delta_3\left(\frac{3}{U}\frac{dU}{dx} + \frac{2}{U}\frac{\delta_H}{\delta_3}\frac{dU}{dx} - M^2 + \frac{1}{r}\frac{dr}{dx}\right) = \frac{2}{\rho_r U^3}\int_0^{\delta} \tau\left(\frac{\partial u}{\partial y}\right)^2 dy = \frac{2D}{\rho_r U^3} = c_D \qquad (18)$$

where *x,y* are the tangential and normal surface coordinates respectively, c_D is the energy losses coefficient, δ_H is the enthalpy thickness, δ_1 the displacement thickness, δ_2 the momentum thickness, δ_3 the energy thickness, ρ_r the density, *r* the radius for axisymmetric bodies, *M* the local Mach number, *U* the local flow velocity at exterior limit of the boundary layer and τ_w is the surface shearing stress.

With the potential distribution of *U(x)* derived, the integral equations of the boundary layer are solved and the distribution of the displacement thickness δ_1 along the surface of the airfoil is calculated. The airfoil geometry is modified by adding the displacement thickness to the thickness of the airfoil. Since the surface of the airfoil is nothing but a boundary

condition viewed from panel method point of view, in fact what happens is the displacement of this boundary condition. A second procedure identical to the one described above starts with the modified geometry of the airfoil, and a new distribution of the potential velocity and pressure coefficient is calculated, as well as a new lift coefficient. This iterative procedure can continue for some circles, until the variation of successive lift coefficients is under a prescribed magnitude. The final pressure distribution and lift coefficient as well as the characteristic magnitudes of the boundary layer, computed in this iterative manner, are these which prevail around the airfoil considering viscous compressible flow and therefore the forces which are exerted on the blade section can be determined.

6 Aeroacoustic calculations

The aeroacoustic computational module is targeted to the calculation of the overall amount of the acoustic pressure perceived by an observer. The numerical model, requires the definition of realistic blade geometry, kinematics and the time-dependent pressure distribution on blade surface. The numerical integration of equations (9) and (10) are performed in time domain.

The discretisation of the acoustic integrals implies the use of a panelling method [10,20] which leads to the transformation of the governing equations to algebraic expressions. Thus, each rotor blade is divided into a number of panels in chordwise and spanwise direction, in a flexible manner allowing high geometrical fidelity. The descretisation of blade surface in panel elements links aerodynamic and aeroacoustic computational modules. The panelling resolution adopted by inviscid/viscous blade surface calculations, supplies the aerodynamic data need for a reliable prediction of loading noise emission. The strength of every source generating noise, is approximated over the centre of each panel in order to achieve accordance between aerodynamic data distributions and blade airfoil characteristics. A typical number of 100 panels on each blade surface is used in the numerical procedure giving satisfactory results to the approximation of the noise parameters.

The retarded time determination that is required to evaluate the integrands is performed by means of an iterational procedure, which defines the azimuthal position of each panel in respect to emission time. The iteration begins by setting an initial value of the azimuth angle and calculating the corresponding function $f = t - t - (\bar{x} - \bar{y}/a)$ where $\bar{x}$ and $\bar{y}$ are the observer and the source positions respectively. This procedure is taking place for 40 azimuthal steps per rotor revolution over each panel. The acoustic pressure signature is calculated by summing the corresponding values over each panel for one observer position. Note, that the observer location $\bar{x}$ and observer time t, are fixed during the evaluation. The convergence of the method is achieved by means of a Newton-Raphson formulation.

Time histories of the acoustic pressure perceived by a stationary observer, fixed on a reference frame require transformation of all noise parameters to this frame. The transformation uses four intermediate reference frames successively and is performed using matrix algebra. Time differentiation in respect to emission time is obtained by means of the Savitzky-Golay [11] numerical method. The desired magnitude at a specific point i is found using central differences with four neighbour points and is considered as the value of a least-squared polynomial that best fits these points. The outcoming values are interpolated to obtain the corresponding magnitudes at the centre of each panel.

7 Discussion and results

The described computational procedure incorporating both aerodynamic and aeroacoustic calculations has been combined to a computer code for the evaluation of the physicomathematical models used. Several aerodynamic aspects of rotor blade and wake flowfield and their effects on noise radiation were studied and some indicative diagrams are shown below. Experimental values presented

here have been measured during experimental campaigns conducted in the open-jet anehoic test section of the German-Dutch Wind Tunnel (DNW) at the Netherlands. The configuration employs an 8x6 m contraction section and a 19m long test section surrounded by a large anehoic hall [1]. The rotor model is a 40% geometrically and dynamically scaled model of the four-bladed hingeless BO 105 main rotor with NACA 23012 blade section, 2m rotor radius and 0.121m chord length.

For the present analysis where thickness and loading noise emission is examined, a reliable and high resolution blade surface pressure and loading distribution is necessary. The effect of boundary layer flow on blade section pressure distribution is given in figure 4.

As derived from this diagram, pure potential calculations tent to overestimate the absolute value of chordwise pressure coefficient especially near the leading edge. Introducing viscous effects on potential pressure distribution by the displacement thickness addition, leads to c_p values closer to experimental measurements. This approach is limited to pure subsonic flow regimes due to incompressible potential calculations.

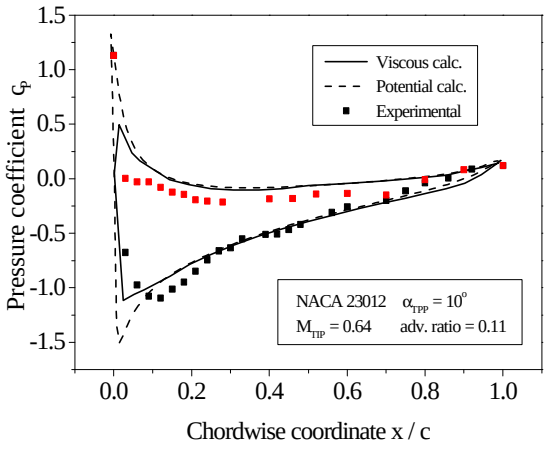

Figure 4. Blade section pressure distribution at 0.75 r/R and 120° azimuth angle

Since the Prandtl-Glauert rule embodied computations is not applicable for high subsonic or transonic flows, the predicted chordwise pressure distribution diverge from experimental results when such flow regimes occur in blade's flowfield. Such cases is not likely to occur for low speed flight conditions regarded by the present analysis.

Another important parameter in wake aerodynamic computations is the applied vortex core modelling. The circulation distribution inside the core region affects the induced velocity field of the vortex. As a result, rotor downwash distribution and the resulting airloading predictions depend on the vortex core model. Since blade load variations is the generating mechanism for loading noise radiation, vortex core model indirectly affects also rotor aeroacoustic calculations. To demonstrate the above statement, Figure 5 presents blade section lift coefficient calculated with two different core models in comparison with experimental data.

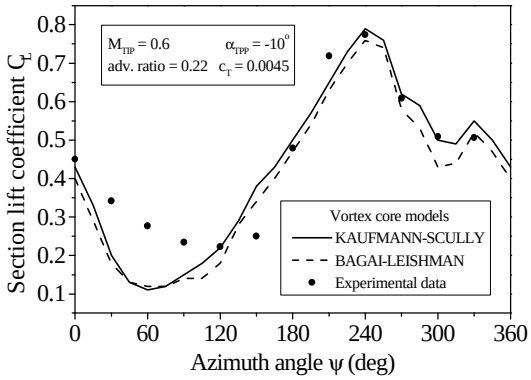

Figure 5. Viscous core modelling effects on computed airload distribution at radial station 0.75 r/R

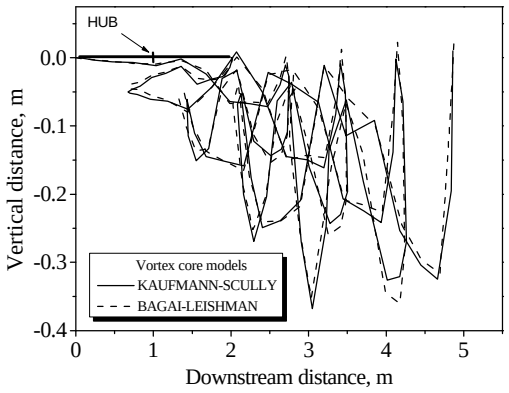

Figure 6. Viscous vortex core effects on computed wake distortion

In the qualitative sketch of Figure 6, the effect of vortex core modelling on the computed distortion of rotor tip vortices is shown. The motion of one tip vortex filament is due to the flowfield induced by itself and its neighbouring vortices. In this way vortex core modelling affects tip vortex spatial location and the resulting interactions with rotor blades.

Blade vortex interactions are known to be responsible for sharp fluctuations of blade airloading and impulsive noise emission. The locations on rotor disk area where such phenomena occur for specific flight conditions is a subject of extensive investigations. Taking advantage of the flexibility provided by free wake analysis, a criterion for the definition of BVI occurrence can be specified as follows. A lower limit of BVI influence can be defined as a percentage of blade downwash changes. In this way, any close encounter between a blade and a vortex segment, which causes a downwash variation that exhibits the prescribed limit, should be considered as strong BVI. By adjusting this limit, the influence of any interaction between blade and the wake vortices can be investigated. With these considerations, a parametric study has been done, in order to define a reasonable limit which affects the computed airloads significantly. Figure 7 presents the results for the specific test case.

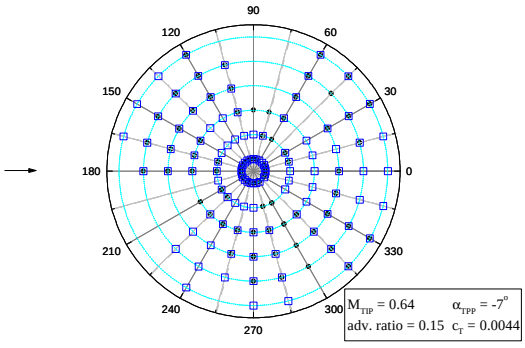

Figure 7. Blade vortex interaction locations on rotor disk

A conclusion that can be derived from the above figure is when this limit is set to a relatively high percent of change, namely 20% (symbol ● denotes 20% changes in induced velocity while □ denotes 5%), the number of BVI which exceed it is reduced considerably. Another conclusion derived from this figure is that the presented methodology predicts increased number of BVI at the forward portion of rotor disk. This is in agreement with the conclusions of other works [24], based on the observation that the tip vortex of one blade, tends to stay closely to rotor disk, till it is forced to move away by the following blade.

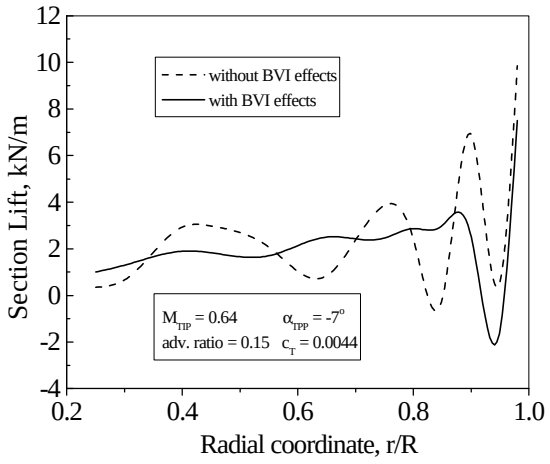

Figure 8. Smoothing of radial airload distribution due to BVI effects at 90° azimuth angle

A phenomenon experimentally observed during BVI is the abrupt change of vortex core radius. Core bursting is suspected to be responsible for the reduction in airload peaks which would be otherwise expected at the advancing side of the rotor. The explanation given, is that after the first blade passage close enough to the tip vortex left by the preceding blade, bursting occurs and is propagated ahead of the blade with higher velocity. In this case the specific blade and the others to follow do not interact with a concentrated vortex line but with a more spread one. As a consequence the changes on blade surface pressure, which result in a sudden airload peak, is not as steep as it would be otherwise. The computed prediction of blade loading distributions showing this effect is given in Figure 8.

Aeroacoustic calculations are based on blade loading variations predicted by the aerodynamic computational procedure

incorporating models for the above-described phenomena. In the next figures numerical results are presented for the standard two-bladed UH-1 helicopter rotor with NACA 0012 profile with 1.829m radius, 0.1334m section chord and 10.9^{o} linear twist. Figure 9 presents the thickness, loading and overall acoustic pressure of a hovering rotor perceived by an inplane observer located in near field. The shape of thickness noise curve is almost symmetrical, while loading noise has a smaller contribution to the overall acoustic pressure, leading to a slight increase of the pressure peak. Figure 10 shows the corresponding sound pressure level near field. This diagram indicates a maximum level of about 130 dBs perceived by the observer.

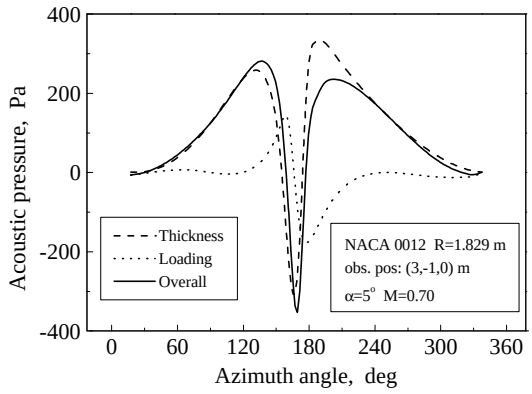

Figure 9. Acoustic pressure distribution for near field observer in hover flight conditions

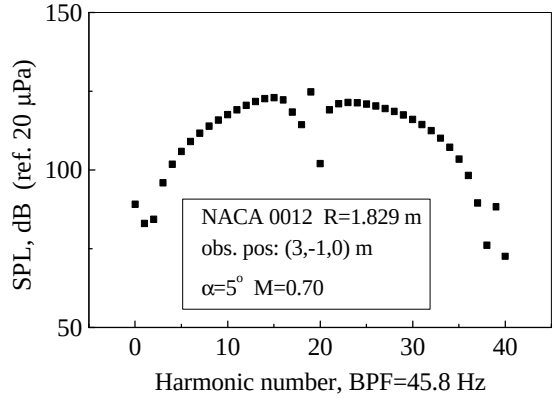

Figure 10. Overall sound pressure level (SPL) in near field

Far field numerical results are shown, for the same test case, in Figures 11 and 12. Acoustic pressure variations show smaller peaks, as expected, while the linear thickness term keeps its symmetrical shape. Sound pressure level results show significant differences for the 20 first harmonics of the blade passage frequency, regarding an approximate difference of 10 dBs between near and far field.

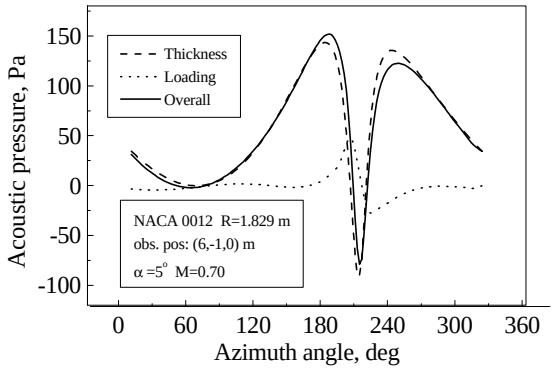

Figure 11. Acoustic pressure distribution for far field observer in hover flight conditions

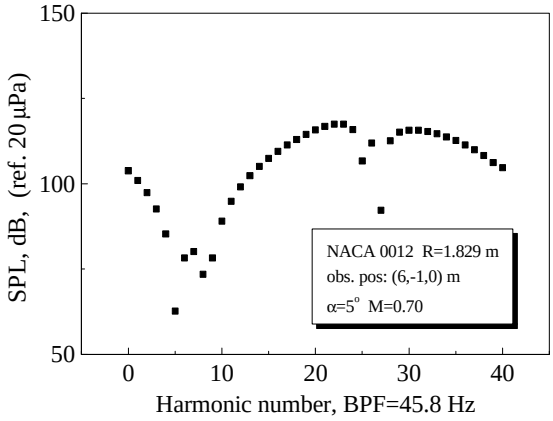

Figure 12. Overall sound pressure level (SPL) in far field

Pressure time histories predicted by the presented computational procedure are compared with experimental data taken during the European HELINOISE aeroacoustic rotor test [25]. Comparisons are shown in Figures 13, 14 for various observer positions and angles of attack. Where available, the agreement with experiments is quite satisfactory.

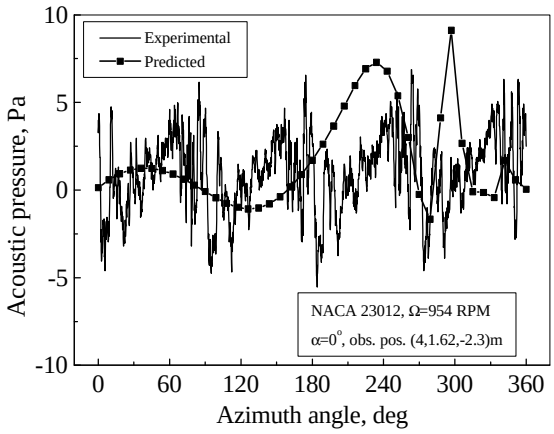

Figure 13. Comparison of the predicted and experimental acoustic pressure for the BO-105 rotor at MT=0.60 at zero angle of attack.

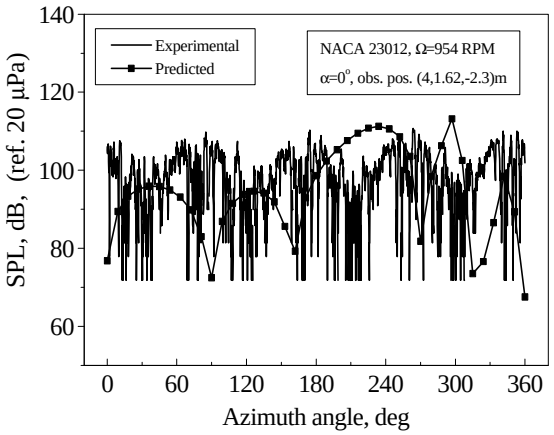

Figure 6. Experimental and theoretical sound pressure level for the BO-105 rotor at MT=0.60 at zero angle of attack

The differences in magnitude do not exceed a maximum of 15% related to a 5dB divergence of sound pressure level. These differences are caused by the simplification of the numerical model which does not take into account specific phenomena occurring mainly at large tip Mach numbers such as turbulence singularities and the delocalisation of the noise sources.

References

[1] Baskin V.Y., Vildgrude L.S., Vozhdayey Y.S., and Maykapar G.I. *Theory of lifting airscrews.* NASA TTF-823,1976.

[2] Beddoes T.S. A wake model for high resolution airloads. *U.S. Army / Amer.Helic.Soc. Int. conf. Rotorcraft Basic Research.* 1985.

[3] Betz A. Verhalten von Wirbelsystemen. *Zeitschr. Angew. Math. Mech. (ZAMM)*, Bd.12, 164-174, 1932.

[4] Bhagwat J.M. and Leishman G.J. Correlation of helicopter rotor tip vortex measurements. *AIAA Journal*. Vol. 38, No. 2, 2000.

[5] Bliss D.B., Teske M.E. and Quackenbush T.R. *A new methodology for free wake analysis using curved vortex elements*. NASA CR-3958, 1987.

[6] Brentner K.S. *Prediction of helicopter discrete frequency noise*. NASA TM 87721, 1986.

[7] Farassat F. and Brentner K.S. The acoustic analogy and the prediction of the noise of rotating blades. *Theoretical and Computational Fluid Dynamics*, No 10, pp. 155-170, 1998.

[8] Farassat F. *Theory of noise generation from moving bodies with an application to helicopter rotors*. NASA TR-R 451, 1975.

[9] Ffowcs-Williams J.E., Hawkings D.L. Sound generation by turbulence and surfaces in arbitrary motion. *Philosophical Transactions of the Royal Society of London.* Series A, 264, No 1151, pp. 321-342, 1969.

[10] Fragias A.P., Spyropoulos A.J., Papanikas D.G. and Margaris D.P. Noise prediction of helicopter rotors under subsonic flight conditions. *Vibration, Noise and Structural Dynamics '99*, Venice, Italy, 1999.

[11] Hamming R.W. *Digital Filters.* 2nd edition, Prentice Hall, 1983.

[12] Heler H., Dobrzynski W., Schultz K.J. and Splettstoesser W.R. Propeller and rotor noise research advances in testing techniques and results. *Proc. Noise and Vibration Conf.* Singapore,1989.

[13] Johnson W. *A comprehensive analytical model of rotorcraft aerodynamics and dynamics*. NASA TM-81182,1980.

[14] Johnson W. *Helicopter theory*. Dover, 1994.

[15] Kaufmann W. Uber die Ausbreitung kreiszlindrischer Wirbel in zahen Flussigkeiten. *Inf. Arch.* Vol.31, No. 1, 1962.

[16] Lamb H. *Hydrodynamics*. 6th Edition, Campridge University Press, 1932.

[17] Leisman G.J., Baker A. and Coyne A. Measurements of rotor tip vortices using three-component laser doppler velocimetry. *Journal of American Helicopter Society*. Vol. 41, No. 4, 1996.

[18] Lighthill G.H. On sound generated aerodynamically, I: General theory. *Philosophical Transactions of the Royal Society of London*, Series A, 221, pp. 564-587, 1952.

[19] McCroskey W.J. and Srinivasan G.R. *Unsteady interactions of transonic airfoils with gusts and concentrated vortices*. AGARD CPP386.

[20] Papanikas D.G., Protopsaltis A. and Pantazis V. Effects of blade and wake characteristics on computed helicopter rotor noise. *14th DGLR/AIAA Aeroacoustics Conference*, Aachen, Germany, 1992.

[21] Papanikas D.G., Spyropoulos A.J., Fertis D.K., Margaris D.P. Helicopter rotor downwash calculation using the vortex element method for the wake modelling. *20th International Conference in Aeronautics.* Sorento Italy, Vol. 2, ICAS-96-1.2.1, pp. 278-289,1996.

[22] Quackenbush T.R., Wachspress D.A. and Boschitsch A.H. Rotor aerodynamic loads computation using a constant vorticity contour free wake model. *AIAA Journal of Aircraft*, Vol. 32, No. 5, 1995.

[23] Schlichting H. *Boundary layer theory*. McGraw Hill, 1979.

[24] Scully M.P. *Computation of helicopter rotor wake geometry and its influence on rotor harmonic airloads.* ASRL TR 178-1, 1975.

[25] Splettstoesser W.R., Niesl G., Cenedese F., Nitti F., and Papanikas D.G. Experimental Results of the European HELINOISE Aeroacoustic Rotor Test. *Journal of American Helicopter Society*, Vol. 40, No. 2, 1995.

[26] Stepniewski W.Z. and Keys N. *Rotary wing aerodynamics*. Dover N.Y., 1984.

[27] Vatistas G.H., Kozel V. and Mih W.C. A simpler model for concentrated vortices. *Experiments in Fluids.* Vol. 11, pp.73-76, 1991.

[28] Windnall S.E. and Wolf T.L. Effect of tip vortex structure on helicopter noise due to blade vortex interactions. *AIAA Journal of Aircraft*, Vol. 17, No. 10, pp. 705-711, 1980.